



Identification and Characterization of Elusive α Precipitates in Cu–Al–Ni Shape Memory Alloys with Combined Electron Microscopy Techniques

F. De Castro Bubani¹ · M. R. Esquivel^{1,2} · R. Gastien³ · E. Zelaya¹

Received: 17 May 2024 / Revised: 12 July 2024 / Accepted: 19 July 2024
© ASM International 2024

Abstract The shape memory effect in Cu–Al–Ni alloys is caused by martensitic transformations between a metastable matrix (β phase) and one or more martensitic phases. In these alloys, when diffusion becomes significant, precipitation of thermodynamically stable α and γ occurs. While several transmission electron microscopy (TEM) works have focused on the characterization of γ , α phase has received minimal attention, likely due to experimental challenges in achieving sufficient TEM image contrast. In this work, we employed a combination of advanced electron microscopy techniques and, for the first time, we were able to identify small α particles with an unprecedented morphology.

Keywords Aging · CuNiAl materials · Austenite · Constrained recovery

Introduction

Thermoelastic martensitic transformations are non-diffusive solid–solid transformations that are behind the recoverable macroscopic shape changes in shape memory alloys (SMAs). These transformations occur at specific temperatures and/or applied stresses [1], which can be adjusted to

optimize the shape memory effect for a given application. For this reason, some SMAs are the subject of commercial interest, e.g., Ni–Ti, which showcases excellent biocompatibility, making it suitable for medical purposes [2, 3].

Cu-based SMAs are economical alternatives to Ni–Ti and offer some additional advantages: Cu–Al–Ni are considered high-temperature SMAs and their martensitic transformation temperatures can be adjusted to around 200 °C, which is higher than most known SMAs. However, these alloys tend to present precipitation of α and/or γ phase during heat treatment at temperatures higher than 100 °C, which poses a challenge to manufacturing processes and potential applications (Fig. 1) [4, 5].

At room temperature, the metastable beta phase has a bcc structure with partial B2 or DO₃ order, depending on the heat treatment applied after solidification. The alpha phase has an fcc structure with a slightly larger lattice parameter than metallic Cu due to the presence of Al atoms [8]. The γ phase has a unit cell of 52 atoms and 2 structural vacancies [9]. It exhibits either an ordered or disordered atomic structure with a lattice parameter that is about three times greater than the lattice parameter of the ordered (B2) β phase.

Even though several published works focus on the characterization of the γ phase, the α phase has received relatively little attention and few studies on α are available in the literature [10–12]. Moreover, published works on the structural characterization of α in Cu–Al–Ni alloys are mostly based on XRD (X-ray diffraction), i.e., not electron diffraction techniques [13–15]. For these works, different methods were used to obtain the alloy, such as melting in a high-frequency induction furnace followed by caliber rolling, spark plasma sintering, and induction melting. Then, the structure obtained was characterized by XRD. By studies on the α phase in Cu–Al-based shape memory alloys, the main characterization technique used is also XRD [16–18]. Moreover,

✉ F. De Castro Bubani
franbubani@gmail.com

¹ Centro Atómico Bariloche (CNEA), CONICET, Av. Bustillo, 9500, R8402AGP Bariloche, Argentina

² Centro Regional Universitario Bariloche, Universidad Nacional del Comahue, Quintral 1250, R8402AGP Bariloche, Argentina

³ Departamento de Materiales y Procesos Estratégicos, DEINSO-CITEDEF, UNIDEF, Juan Bautista de La Salle 4397, Villa Martelli, Buenos Aires, Argentina

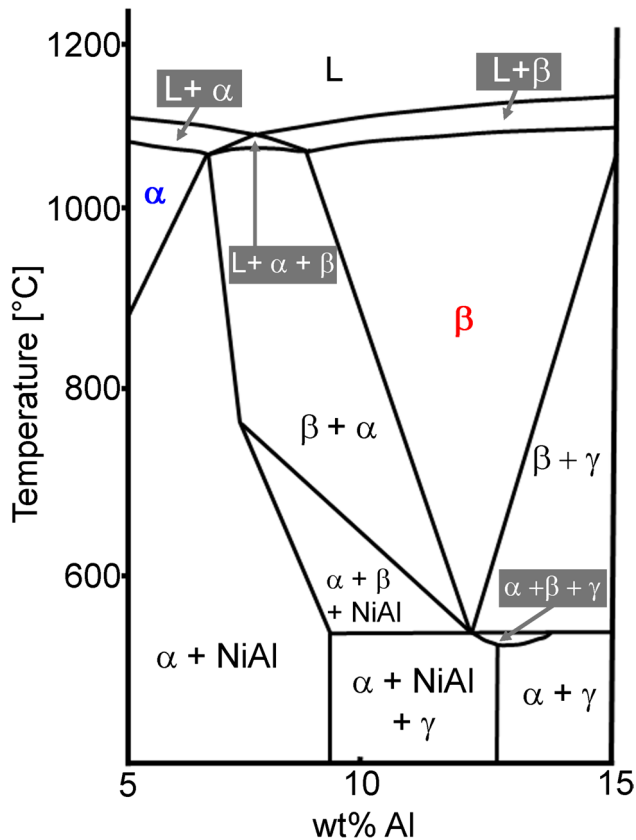


Fig. 1 Vertical cross-section (pseudobinary) at 4-wt.% Ni of the ternary Cu–Al–Ni phase diagram. Modified from [6, 7]. Modified from (Ref. [7]), available under CC BY-NC-ND 4.0 license at Elsevier

not many papers mention the shape or microstructure of the α phase, but authors like Chen and Singh show one or two images of the α phase in a Cu–Al–Ni SMA. Chen et al. show an optical micrograph and a SEM micrograph of “strip-like” polycrystalline α phase formed within the matrix of a Cu–14.1Al–9.0Ni (wt. %) alloy aged at 500 °C [19]. Also, Singh et al. found α phase in a Cu–14-wt. %Al–4-wt.%Ni alloy heated at 550 °C. The dark field image of that sample shows striation perpendicular to [2 0 0] direction [20]. Other authors also found a flat microstructure in SEM and TEM images of Cu–Al-based shape memory alloys obtained by milling [21, 22] or in Cu–Al–Ni shape memory alloys under high-temperature heat treatments (higher than 380 °C) [23, 24]. However, none of the authors that report the α microstructure presents a thorough characterization of this phase in a Cu–Al–Ni SMA with heat treatments near 200 °C.

Microstructural features like the shape, size, and concentration of α and γ precipitates significantly influence the macroscopic behavior of the alloy [9, 10]. This influence is particularly evident in the shape memory effect, which can be substantially compromised by extensive

precipitation. For this reason, not only is it important to find out which heat treatment produces precipitation of α and γ phases, but it is also important to characterize the shape, size, and concentration of those precipitates.

In this work, we characterize the structure and microstructure of α phase precipitates by employing various transmission electron microscopy (TEM) techniques in a Cu–14.3Al–4.1Ni (wt.%) SMA after thermal treatments at 200 °C. To elucidate the mechanisms by which thermal treatments hinder martensitic transformation, a comprehensive understanding of precipitate morphology and the interplay between precipitate structure and the β matrix is crucial.

Materials and Methods

The alloy was prepared from high-purity (99.9%) Cu, Al, and Ni in a two-step process designed to minimize composition shifts. First, Cu and Ni were melt together in an inductive furnace with controlled Ar atmosphere. Second, the Al content was added to the previous Cu–Ni binary alloy and melted in a resistance furnace with Ar atmosphere. As a result, a Cu–14.3Al–4.1Ni (wt.%—nominal composition) ternary alloy was obtained. Then, a single crystal was grown by the Bridgman technique (further details are available in [25]), annealed at 930 °C for 1 h, and quenched in a mixture of water and ice. Two cylindrical rods were cut with their longitudinal axes near [001] _{β} . One rod was treated for 36.5 h at 200 °C and the other for 7.5 h at the same temperature.

Two 3-mm diameter samples were cut from each cylindrical rod using a low-speed diamond wheel saw and then mechanically ground to a thickness of 0.2 mm. Further thinning was performed by electropolishing using a TENUPOL double-jet equipment at $T=10$ °C and $V=12$ V. A solution of 5-g urea, 250-ml ethyl alcohol, 50-ml propyl alcohol, 250-ml orthophosphoric acid, and 500-ml distilled water was used as electrolyte.

The scanning electron microscopy (SEM) observations were performed in a thermionic FEI Inspect s50 microscope operated between 1 and 30 kV.

The transmission electron microscopy (TEM) observations were carried on in a field emission TECNAI F20 G2 microscope operated at 200 kV and equipped with a Gatan Quantum ER electron energy loss spectroscopy (EELS) system. The Gatan imaging filter allows the acquisition of images using zero-loss peak energy filtering (ZLP), which improves selected area diffraction and microdiffraction patterns of thick zones of the sample by filtering out inelastic scattered electrons [26].

Results and Discussion

A sample under 36.5 h of thermal treatment was observed in TEM mode and a characteristic microstructure with dislocations and prismatic precipitates with approximately 40-nm edge length was identified, as reported in previous works [27]. However, scanning transmission electron microscopy (STEM) images of the same sample revealed bright cruciform defects in the thicker parts of the sample. These defects have an average size of 1.5 μm , which is almost two orders of magnitude greater than the defects observed in TEM mode (40 nm). However, the microstructure could not be clearly identified in STEM because in these areas the sample is considerably thick, which is a limitation that also arises in TEM mode. However, the diffraction patterns of a selected area on one of the defects presents some extra reflections in $[001]_{\beta}$ zone axis. These extra spots can be indexed consistently considering two twin variants of α phase in the $[101]_{\alpha}$

zone axis (Fig. 2). Moreover, in this figure, the ratio between the $1\ 1\ 1_{\alpha}$ spot and $1\ 1\ 0_{\beta}$ spot is 1, within the experimental error. This implies a very low level of deformation in the material, which is due to the coherency of the structures.

The microstructure could not be clearly identified due to the large thickness of the sample, so only SEM images were taken. Figure 3 a shows a secondary electron image of the cruciform defect. The image was obtained at a working distance of 2.5 mm at 5 kV. In this image mode and under these experimental conditions, secondary electrons type I (SE1) are mainly used in order to optimize spatial resolution. Here it can be noticed that each arm of the cross, i.e., the defect has structures that resemble dendritic growth. The same kind of morphology was observed in Cu dendrites [28], in Cu–Al, and Cu–Zn–Al alloys. However, in Cu–Al and Cu–Zn–Al alloys, the dendrites were identified as γ phase [29, 30], which differs from our findings. In order to better characterize the defects, two electron diffraction scattering

Fig. 2 **a** Selected area diffraction of the sample heated for 36.5 h at 200 °C. The sample was in the $[001]_{\beta}$ zone axis. **b** Key diagram with two twin variants of the α phase in the $[101]_{\alpha}$ zone axis and the β phase in the $[001]_{\beta}$ zone axis. The twin plane is along the $[11-1]_{\alpha}$ direction for both variants

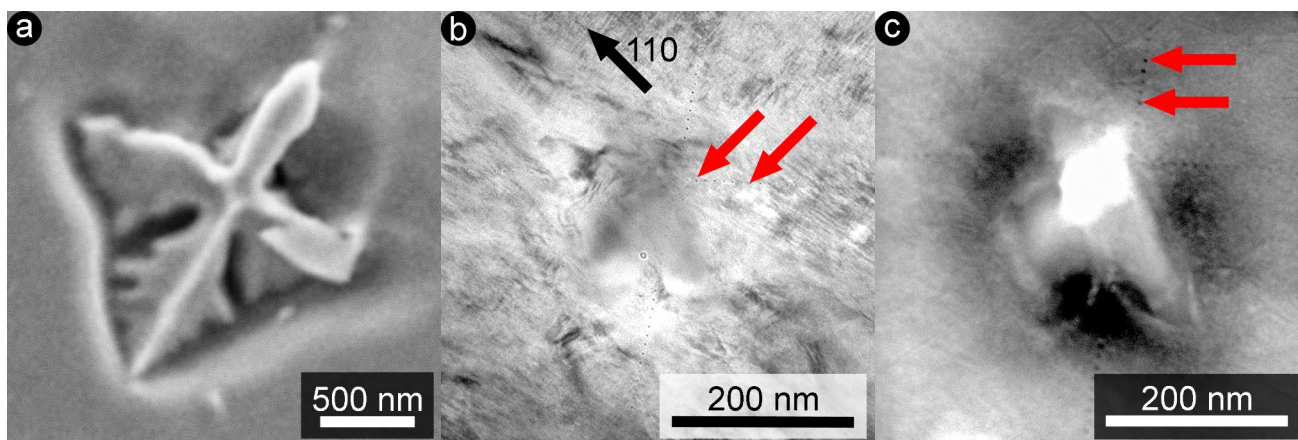
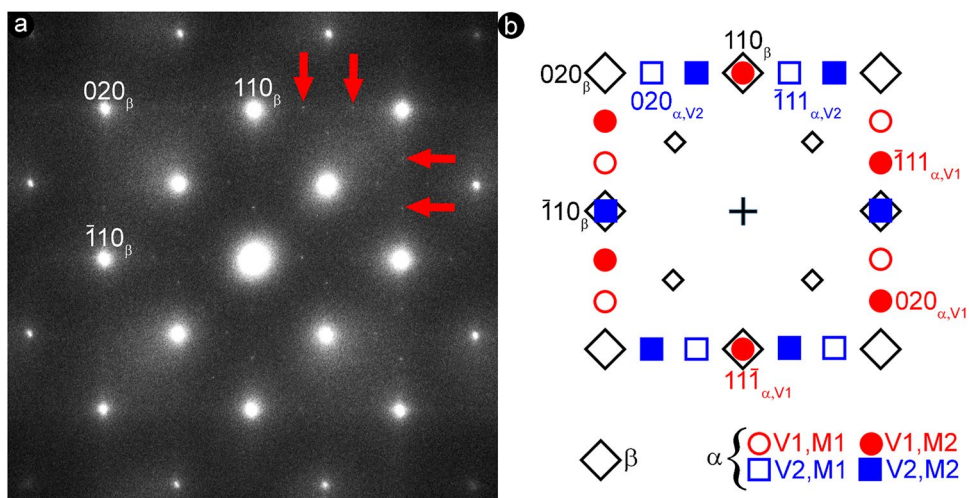


Fig. 3 **a** Secondary electrons (SE) SEM image of a defect in a sample heated for 36.5 h at 200 °C. **b** Bright field image of a defect in a sample heated for 7.5 h at 200 °C. **c** STEM image of the same defect shown in **b**

(EDS) point measurements were taken, one on the defect and the other on the matrix next to it, both at 5 kV. However, the number of counts corresponding to the Al peak in both measurements is very similar when experimental errors are taken into account. It occurs due to the interaction between secondary electrons and the sample. Even when a small spot size is used at 5 kV, the interaction zone in the sample has a diameter of around 1.5 μm [31]. Since none of the defects of the sample were much larger than 1.5 μm , no compositional difference could be detected by SEM EDS.

Another sample with 7.5 h of thermal treatment was analyzed. This sample reveals smaller cruciform defects in STEM mode (measuring around 1 μm). However, these defects were not easily detectable in TEM mode. The size of the defect and the low elastic deformation produced in the matrix due to the presence of these defects makes their detection in TEM imaging very difficult. The same cruciform defect can be seen in TEM and STEM mode in Fig. 3b, c. Here, it can be noticed that the protuberances of the defect are aligned along the $[110]_{\beta}$ direction. An EDS line scan was performed over this defect (red arrows indicate the marks left by each EDS measurement point) and an increase in Cu counts was detected. However, the number of counts in the defect are between two and three times greater than in the matrix next to it. This results in a screening effect that makes it impossible to obtain a reliable quantification. For this reason, we present a point EDS analysis of the defect shown in Fig. 4. In this figure, there are four different areas of interest (points 1, 2, 3, and 4) and each measurement was taken during 100 s. In Point 1, in the brighter zone of the defect, the number of counts was two times greater than point 3, but several models of quantification show the same Cu/Al ratio in both measurements. On the other hand, point 3 and point

4 produced a similar number of counts for the same acquisition time, but the K Al peak at point 3 (the matrix) is greater than the K Al peak at point 4 (the cruciform defect). Moreover, the counts under the Al K peak obtained at point 2 are almost undetectable. Point 2 was placed over a defect next to the cruciform defect that presents the same brighter contrast. With a camera length of 90 mm in STEM mode, cruciform defects and the smaller defects around them present brighter contrast, which is caused by differences in chemical composition and is compatible with more Cu content in them.

The defects around the cruciform defect have irregular shapes and measure between 40 and 100 nm. Their microstructure is consistent with stacking faults along the $[110]_{\beta}$ direction. Figure 5 shows an EDS line scan across one of these small defects. Here, an increase in Cu content can also be detected. EDS results and STEM images of both kinds of defects (cruciform and smaller defects) indicate that the composition is consistent with a phase richer in Cu content, i.e., EDS results suggest the presence of the α phase [6].

In order to better determine the structure of the defects, a high-resolution transmission electron microscopy (HRTEM) image was analyzed. Figure 6a shows two small defects with brighter contrast than the matrix in a STEM image. Striation along the $[110]_{\beta}$ direction can be clearly distinguished, as in the defect shown in Fig. 5. In addition, the bright field image of the same defects in the $[001]_{\beta}$ zone axis reveals similar contrast (Fig. 6b). The HRTEM image shows the characteristic ABC stacking sequence of an FCC structure in the $[101]_{\text{fcc}}$ zone axis (Fig. 6c). In other words, the HRTEM image shows a stacking sequence consistent with the α phase in these kind of alloys [31].

Even though the SAD pattern of Fig. 2 in the $[001]_{\beta}$ zone axis is consistent with the presence of two twin variants in

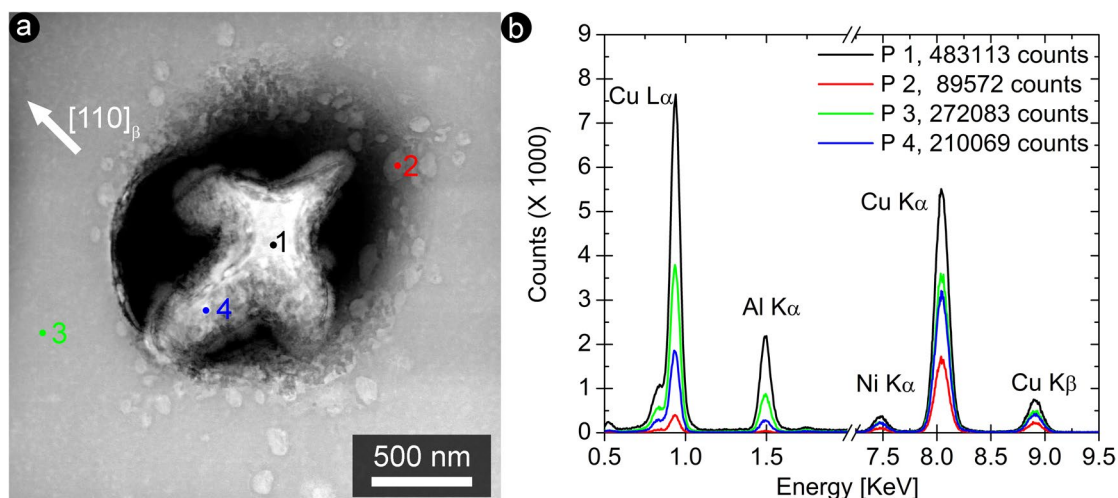


Fig. 4 **a** STEM image of a sample heated for 7.5 h at 200 $^{\circ}\text{C}$, with 90-mm camera length. A cruciform defect surrounded by smaller defects can be detected due to Z contrast. **b** EDS performed for 100 s in each point shown in **a**

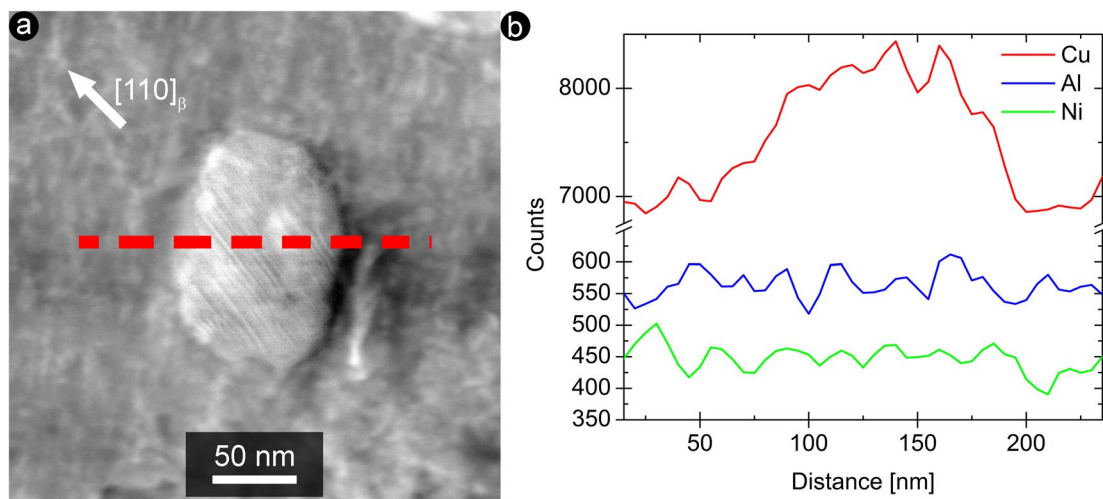
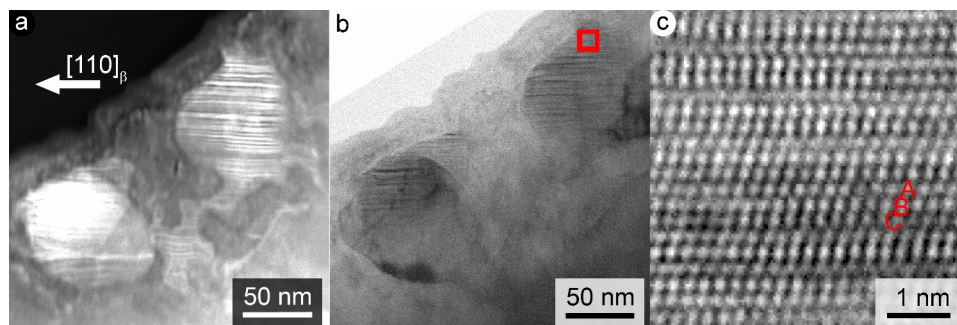


Fig. 5 STEM image of a small defect taken with a camera length of 90 nm. **b** Line scan along the red dash line indicated in **a**. A significant increase in Cu content can be seen

Fig. 6 **a** STEM image of a sample heated for 7.5 h at 200 °C taken with a camera length of 90 nm. Bright field image of the same area shown in **a**. **c** HRTEM image of the zone inside the red square in **b**. The characteristic ABC sequence can be clearly distinguished



the $[101]_{\alpha}$ zone axis, the same extra spot could be interpreted as a stronger γ reflection in $[001]_{\gamma}$ [32, 33], which leads to ambiguity in the identification of which phase (α or γ) is present in the defect. For this reason, energy-filtered microdiffraction was performed near the tip of one protuberance of a cruciform defect. Figure 7 shows microdiffraction in the matrix next to the cruciform defect and in the defect itself. A slit filter of 10 eV centered on the zero-loss peak filters out the inelastically scattered electrons, which are significant because the defect and the matrix next to it are considerably thick. The microdiffraction was performed with a 6-nm beam and reflections of the defect and the matrix were captured. The indexation of the spots produced by the defect is consistent with the presence of one α phase twin variant in the $[101]_{\alpha}$ zone axis, which eliminates all ambiguity and definitively demonstrates the presence of α . Once again, the $1\ 1\ 0_{\beta}$ spot of the matrix coincides with the $-1\ -1\ 1_{\alpha}$ spot of the defect, within experimental errors. These results and the low contrast of the cruciform defect indicate that elastic deformation is very low, which is a consequence of the coherence of the structures.

Conclusion

Defects with a morphology that had never been reported were discovered in Cu–14.3-wt%Al–4.1-wt%Ni samples annealed at 200 °C.

The defects have variations in size and shape in the same sample, which suggests different stages of nucleation and growth.

The bigger defects appear cruciform in TEM imaging but in fact have six protuberances along the $[110]_{\beta}$ direction, as a result of its cubic symmetry. Each point studied seems to contain two variants of the α phase.

Both the chemical composition and the structure of the defects are compatible with the α phase.

The α defects and the β matrix seem coherent, which results in very low elastic deformation.

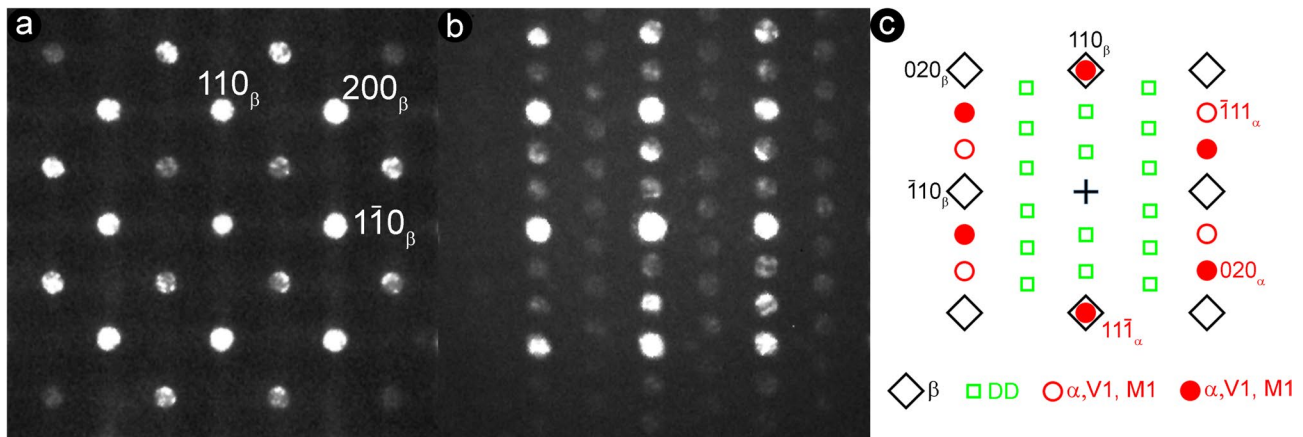


Fig. 7 **a** Filtered microdiffraction pattern of the matrix next to an α precipitate of a sample heated for 7.5 h at 200 °C. **b** Filtered microdiffraction pattern of the α precipitate. The key diagram of the **b** pat-

tern is shown in **c**. One twinned variant with a $[101]_{\alpha}$ zone axis parallel to $[001]_{\beta}$ zone axis can be observed

Acknowledgements Financial support from ANPCyT PICT-2021-GRF-TI-00015 and CONICET PUE 018/18—Argentina is acknowledged. We gratefully acknowledge M. Mosquera Panizo for performing the heat treatments of the samples.

Data availability The authors declare that all data generated or analyzed during this study is included in this published article.

References

- Otsuka K, Shimizu K (1986) Pseudoelasticity and shape memory effects in alloys. *Int Met Rev*. <https://doi.org/10.1179/imtr.1986.31.1.93>
- Shabalovskaya S, Van Humbeeck J (2008) Biocompatibility of Nitinol for biomedical applications. *Shape Mem Alloys Biomed Appl*. <https://doi.org/10.1533/9781845695248.1.194>
- Kumar Patel S, Behera B, Swain B, Roshan R, Sahoo D, Behera A (2020) A review on NiTi alloys for biomedical applications and their biocompatibility. *Mater Today* 33:5548–5555. <https://doi.org/10.1016/j.matpr.2020.03.538>
- Gastien R, Corbellani CE, Bozzano PB, Sade M, Lovey FC (2010) Low temperature isothermal aging in shape memory CuAlNi single crystals. *J Alloys Compd* 495:428–431. <https://doi.org/10.1016/j.jallcom.2009.10.100>
- Zárubová N, Gemperle A, Novák V (1997) Initial stages of γ_2 precipitation in an aged Cu–Al–Ni shape memory alloy. *Mater Sci Eng A* 222(2):166–174. [https://doi.org/10.1016/S0921-5093\(96\)10520-7](https://doi.org/10.1016/S0921-5093(96)10520-7)
- Dunne DP, Kennon NF (1981) Ageing of copper-based shape memory alloys. *Met Forum* 4:176–183
- Abolhasani D, Han SW, VanTyne CJ, Kang N, Moon YH (2021) Enhancing the shape memory effect of Cu–Al–Ni alloys via partial reinforcement by alumina through selective laser melting. *J Market Res* 15:4032–4047. <https://doi.org/10.1016/j.jmrt.2021.10.040>
- Swann PR, Warlimont H (1963) The electron-metallography and crystallography of copper-aluminum martensites. *Acta Metall* 11(6):511–527. [https://doi.org/10.1016/0001-6160\(63\)90086-5](https://doi.org/10.1016/0001-6160(63)90086-5)
- Westman S (1965) Refinement of the gamma-Cu9Al4 structure. *Acta Chem Scand* 19:1411–1419. <https://doi.org/10.3891/acta.chem.scand.19-141>
- Araujo VEA, Gastien R, Zelaya E, Beiroa JI, Corro I, Sade M, Lovey FC (2015) Effects on the martensitic transformations and the microstructure of CuAlNi single crystals after ageing at 473 K. *J Alloys Compd* 641:155–161. <https://doi.org/10.1016/j.jallcom.2015.04.065>
- Gastien R, Corbellani CE, Araujo VEA, Zelaya E, Beiroa JI, Sade M, Lovey FC (2013) Changes of shape memory properties in CuAlNi single crystals subjected to isothermal treatments. *Mater Charact* 84:240–246. <https://doi.org/10.1016/j.matchar.2013.08.008>
- Cheniti H, Bouabdallah M, Patoor E (2009) High temperature decomposition of the β_1 phase in a Cu–Al–Ni shape memory alloy. *J Alloys Compd* 476:420–424. <https://doi.org/10.1016/j.jallcom.2008.09.003>
- Yu J, Zhang J, Wang Q, Yu H, Zheng T, Yin F (2023) Effect of caliber rolling on microstructures and properties of an inoculated Cu–Al–Ni shape memory alloy. *Intermetallics* 162:10802. <https://doi.org/10.1016/j.intermet.2023.108021>
- Portier RA, Ochin P, Pasko A, Monastyrsky GE, Gilchuk AV, Kolomytsev VI, Koval YN (2013) Spark plasma sintering of Cu–Al–Ni shape memory alloy. *J Alloys Compd* 577S:S472–S477. <https://doi.org/10.1016/j.jallcom.2012.02.145>
- Chentouf SM, Bouabdallah M, Gachon J-C, Patoor E, Sari A (2009) Microstructural and thermodynamic study of hypoeutectoidal Cu–Al–Ni shape memory alloys. *J Alloys Compd* 470:507–514. <https://doi.org/10.1016/j.jallcom.2008.03.009>
- Pascal NNS, Giordana MF, Napolitano F, Esquivel MR, Zelaya E (2017) Thermal stability analysis of Cu–11.8 wt%Al milled samples by TEM and HT-XRD. *Adv Powder Technol* 28(10):2605–2612. <https://doi.org/10.1016/j.apt.2017.07.012>
- Sari U, Kirindi T, Ozcan F, Dikici M (2011) Effects of aging on the microstructure of a Cu–Al–Ni–Mn shape memory alloy. *Int J Miner Metall Mater* 18(4):430–436. <https://doi.org/10.1007/s12613-011-0458-1>
- Adorno AT, Guerreiro MR, Silva RAG (2003) Aging kinetics in the Cu–8 wt.% Al alloy with Ag additions. *J Alloys Compd* 354:165–170. [https://doi.org/10.1016/S0925-8388\(03\)00020-3](https://doi.org/10.1016/S0925-8388(03)00020-3)

19. Chen CH, Yang CC, Liu TF (2003) Phase transition in a Cu-14.1Al-9.0Ni alloy. *Mater Sci Eng A* 354:377–386. [https://doi.org/10.1016/S0921-5093\(03\)00041-8](https://doi.org/10.1016/S0921-5093(03)00041-8)
20. Singh J, Chen H, Wayman CM (1986) Transformation sequence in a Cu-Al-Ni shape memory alloy at elevated temperatures. *Metall Trans A* 17(1):65–72. <https://doi.org/10.1007/BF02644443>
21. Deng Z, Yin H, Zhang C, Zhang G, Li W, Zhang T, Zhang R, Jiang X, Qu X (2019) Microstructure and mechanical properties of Cu–12Al–xNi alloy prepared using powder metallurgy. *Mater Sci Eng A* 759:241–251. <https://doi.org/10.1016/j.msea.2019.05.051>
22. Giordana MF, Esquivel MR, Zelaya E (2015) A detailed study of phase evolution in Cu–16 at. %Al and Cu–30 at. %Al alloys under different types of mechanical alloying processes. *Adv Powder Technol* 26(2):470–477. <https://doi.org/10.1016/j.apt.2014.12.005>
23. Bouabdallah M, Baguenane-Benalia G, Saadi A, Cheniti H, Gachon JC, Patoor E (2013) Precipitation sequence during ageing in $\beta 1$ phase of Cu–Al–Ni shape memory alloy. *J Therm Anal Calorim* 112:279–283. <https://doi.org/10.1007/s10973-012-2837-x>
24. Sun YS, Lorimer GW, Ridley N (1990) Microstructure and its development in Cu–Al–Ni alloys. *Metall Trans A* 21:575–588. <https://doi.org/10.1007/BF02671930>
25. Guilemany JM, Gil FJ, Miguel JR (1988) Preparation and characterization of single crystals of copper based shape memory alloys. *Rev Metal Madrid* 24(3):175–179
26. Williams DB, Carter CB (2009) *Transmission electron microscopy*. Springer, New York. <https://doi.org/10.1007/978-0-387-76501-3>
27. Panizo MM, de Castro BF, Gastien ACR (2021) Microstructure and thermo-mechanical properties after recovering treatments in aged CuAlNi shape memory alloys. *Shap Mem Superelast* 7(3):414–421. <https://doi.org/10.1007/s40830-021-00341-2>
28. Nikolić ND, Živković PM, Pavlović MG, Baščarević Z (2019) Overpotential controls the morphology of electrolytically produced copper dendritic forms. *J Serb Chem Soc* 84(11):1209–1220. <https://doi.org/10.2298/JSC190522066N>
29. Husain SW, Ahmed MS, Qamar I (1999) Dendritic morphology observed in the solid-state precipitation in binary alloys. *Metall Mater Trans A* 30(6):1529–1534. <https://doi.org/10.1007/s11661-999-0089-6>
30. Castro ML, Fornaro O (2009) Formation of dendritic precipitates in the beta phase of Cu-based alloys. *J Mater Sci* 44:5829–5835. <https://doi.org/10.1007/s10853-009-3821-0>
31. Goldstein JI, Newbury DE, Michael JR, Ritchie NWM, Henry J, Scott J, Joy DC (2017) *Scanning electron microscopy and X-ray microanalysis*. Springer, New York. <https://doi.org/10.1007/978-1-4939-6676-9>
32. Zelaya E, Schryvers D (2010) FCC surface precipitation in Cu–Zn–Al after low angle Ga⁺ ion irradiation. *Mater Trans* 51(12):2177–2180. <https://doi.org/10.2320/matertrans.M2010171>
33. Zelaya E, Schryvers D, Tolley A, Fitchner PFP (2010) Cavity nucleation and growth in Cu–Zn–Al irradiated with Cu⁺ ions at different temperatures. *Intermetallics* 18(4):493–498. <https://doi.org/10.1016/j.intermet.2009.09.010>

Publisher's Note Springer Nature remains neutral with regard to jurisdictional claims in published maps and institutional affiliations.

Springer Nature or its licensor (e.g. a society or other partner) holds exclusive rights to this article under a publishing agreement with the author(s) or other rightsholder(s); author self-archiving of the accepted manuscript version of this article is solely governed by the terms of such publishing agreement and applicable law.